Simulation of a topological phase transition in a Kitaev chain with long-range coupling using a superconducting circuit

Ziyu Tao,[*] Tongxing Yan,[*] Weiyang Liu,[*] Jingjing Niu, Yuxuan Zhou, Libo Zhang, Hao Jia, Weiqiang Chen, Song Liu,[†] Yuanzhen Chen,[‡] and Dapeng Yu

Institute for Quantum Science and Engineering and Department of Physics, Southern University of Science and Technology, Shenzhen 518055, China

(Received 16 August 2019; published 8 January 2020)

We report an experimental work on simulating the Kitaev chain of one-dimensional *p*-wave superconductivity with long-range coupling using superconducting quantum circuits. The effective Hamiltonian of this model in the momentum space is mapped onto that of a qubit driven by a tunable microwave control field. By monitoring the dynamics of the qubit, we generate intuitive yet precise visualization of topological characteristics of different quantum phases of the system. Topological invariants can be directly deduced from the experimental results, without relying on indirect extraction from measurements such as microwave spectroscopy and temporal averaging. Therefore a much enhanced efficiency of measurement can be realized compared to other methods that are often used to simulate topological phase transitions. As a consequence, a comprehensive phase diagram covering a wide range of the parameter space is obtained. Topological phase transitions and quantum multicritical points are clearly demonstrated. In particular, new topological phases emerge as a consequence of long-range coupling. The method used here can be readily generalized to simulate more complex systems on different experimental platforms.

DOI: 10.1103/PhysRevB.101.035109

I. INTRODUCTION

The Kitaev chain of a one-dimensional *p*-wave superconducting wire represents one of the simplest models exhibiting symmetry-protected topological (SPT) order [1–3]. Depending on the relative strength of the chemical potential and magnitudes of hopping and pairing of Cooper pairs, the system assumes different topological phases that can be differentiated by the number of Majorana zero-energy modes localized at the open boundaries of the chain [4,5]. The Kitaev chain can also be mapped onto the one-dimensional transverse field Ising model (TFIM), which is an exemplary system for the study of quantum phase transition and quantum criticality [6–8]. The topological phases discussed above can be directly linked to ferromagnetic and quantum disordered phases in the TFIM, respectively. More recently, there has been substantial interest in the generalization of the Kitaev model to include long-range coupling [6–20]. Theoretical studies taking into account such coupling have yielded many intriguing new results. Among them are the emergence of new phases that are topologically nontrivial and possibly beyond the current SPT classification [7,17], topological phase transitions without closing a gap [11], weakened bulk-edge correspondence [17], massive Majorana zero-energy modes [16,19], violation of the area law of the von Neumann entropy [11,17], and so on.

Simulation of quantum many-body systems such as the Kitaev chain and the Ising model is important motivation for the research of quantum computation and simulation. Direct simulation of targeted models usually involves sophisticated engineering of the Hamiltonian of a tunable system constructed using, for example, cold atoms [21], trapped ions [22–25], molecules in NMR experiments [26], or superconducting qubits [27–30]. Simulation done in this way requires scalability and high-precision control, which are technically challenging for today's technology. Alternative methods have thus been proposed for certain simplified scenarios. One particularly interesting case arises if the Hamiltonian of a targeted many-body system can be exactly diagonalized in the momentum space. In this case, a single qubit is sufficient for simulating the system. Implementations of this idea in various ways, such as via adiabatic evolution, Autler-Towns splitting, and quantum quench, have been used to simulate a variety of topological matters and topological phase transitions [31–38].

The majority of existing experimental work on simulating the Kitaev chain and the Ising model concern only short-range coupling or interaction, i.e., nearest-neighbor (NN) hopping and pairing of Copper pairs (the Kitaev chain) or NN interaction between spins (TFIM). In a few exceptional experiments conducted with trapped ions [25,39–42], long-range interaction was generated via sophisticated laser-induced manipulation of the internal vibrational modes of the ions. In general, the tunability of relevant control parameters was rather limited compared to what one would desire.

In this work, we report an experiment that simulates the Kitaev chain with long-range coupling using superconducting quantum circuits. By monitoring the evolution of a qubit driven by precisely designed and tunable microwave pulses, we map out the effective Hamiltonian of the Kitaev chain with both NN and next-nearest-neighbor (NNN) coupling in

[*]These authors contributed equally to this work.
[†]lius3@sustech.edu.cn
[‡]chenyz@sustech.edu.cn

momentum space. The topological invariant of the Hamiltonian is directly extracted from the experimental data. By performing such measurements with several varied control parameters, we obtain a comprehensive phase diagram where topological phase transitions and quantum multicritical points are clearly demonstrated. In particular, a new topological phase emerges as a result of the presence of the NNN coupling, which supports two Majorana zero-energy modes on each end of the chain.

Our method generates intuitive yet precise visualizations of topological characteristics of the system under study. It does not rely on indirect measurements that use, for example, microwave spectroscopy or extended time averaging. In addition, as explained later, we implement the concept of "shortcut to adiabaticity" to overcome the shortcoming of long runtime associated with adiabatic evolutions. These two factors combined lead to a much enhanced efficiency of measurement compared to other methods that are often used to simulate topological phase transitions using artificial quantum systems. As a result, we are able to map out a phase diagram in wide ranges of the control parameters, rather than only focusing on a few demonstrative points in the parameter space, typical in other methods.

II. THEORY

The Hamiltonian of the one-dimensional Kitaev chain with both NN and NNN coupling can be written in the following form:

$$H = -\mu \sum_{i=1}^{N} c_i^\dagger c_i - \lambda_1 \sum_{i=1}^{N-1} (c_i^\dagger c_{i+1} + c_i c_{i+1} + \text{H.c.}) - \lambda_2 \sum_{i=2}^{N-1} (c_{i-1}^\dagger c_{i+1} + c_{i+1} c_{i-1} + \text{H.c.}). \quad (1)$$

Here μ is the chemical potential, and λ_1, λ_2 are the NN and NNN hopping and pairing strength, respectively. In momentum space, the corresponding effective Hamiltonian is $H(k) = \vec{d}(k) \cdot \vec{\sigma}$, where the Anderson pseudospin vector $\vec{d}(k) = (d_x, d_y, d_z) = (0, 2\lambda_1 \sin k + 2\lambda_2 \sin 2k, -2\lambda_1 \cos k - 2\lambda_2 \cos 2k - \mu)$ and Pauli matrices $\vec{\sigma} = (\sigma_x, \sigma_y, \sigma_z)$. $H(k)$ has a chiral symmetry as $\sigma_x H(k) \sigma_x^{-1} = -H(k)$ and falls into the BDI class of the tenfold classification of one-dimensional gapped systems [2]. It preserves the Z-type topology, and the topological invariant is simply the winding number of $\vec{d}(k)$ in an auxiliary space as k is varied in the first Brillouin zone $[0, 2\pi]$ [see Fig. 1(a)]. The winding number can be calculated as $\mathcal{W} = \oint d\theta(k)/2\pi$, where $\theta(k)$ is the orientation angle of $\vec{d}(k)$ and the integration is carried out over the first Brillouin zone. Furthermore, the number of Majorana zero-energy modes in each phase supported by $H(k)$ is equal to the topological invariant of that phase.

The effective Hamiltonian $H(k)$ can be readily simulated by a single qubit under an external drive $\vec{B}(t)$:

$$H(k) = \vec{d}(k) \cdot \vec{\sigma} \leftrightarrow H(t) = \vec{B}(t) \cdot \vec{\sigma}. \quad (2)$$

A straightforward way is to set the external drive $\vec{B}(t)$ to be $\vec{d}(k)$. In order to do that, we link the momentum k to the evolution time t by setting $t = kT/\pi \in [0, 2T]$. As t evolves from 0 to $2T$, k varies from 0 to 2π, and the time-dependent Hamiltonian $H(t) = \vec{B} \cdot \vec{\sigma} = \vec{d}(k(t)) \cdot \vec{\sigma}$ undergoes a cyclic evolution, mapping out $H(k(t))$ in the first Brillouin zone. The two instantaneous eigenstates of $H(t)$, indicated by red and green arrows in Fig. 1(b), faithfully follow $H(t)$ during the evolution. If such an evolution is adiabatic and the qubit is initialized into one of the eigenstates of $H(t = 0)$, the qubit will stay in the corresponding instantaneous eigenstate during the evolution. In other words, the state vector of the qubit will also faithfully follow $H(t)$. In the current case, since $H(t)$ has only y and z components, the qubit will also evolve in the yz plane of the Bloch sphere. Therefore the state of the qubit can be determined by simply measuring the expectation values of $\langle \sigma_y \rangle$ and $\langle \sigma_z \rangle$, rather than performing a standard quantum state tomography measurement. Using such a relation between the state of the qubit and $H(k)$, one can deduce the topological properties of $H(k)$ by observing the evolution of the qubit as k is varied. For example, the winding number $\mathcal{W}$ of the pesudospin $\vec{d}(k)$ will be the same as the number of completed circles of the qubit rotating in the yz plane of the Bloch sphere [see Fig. 1(c)].

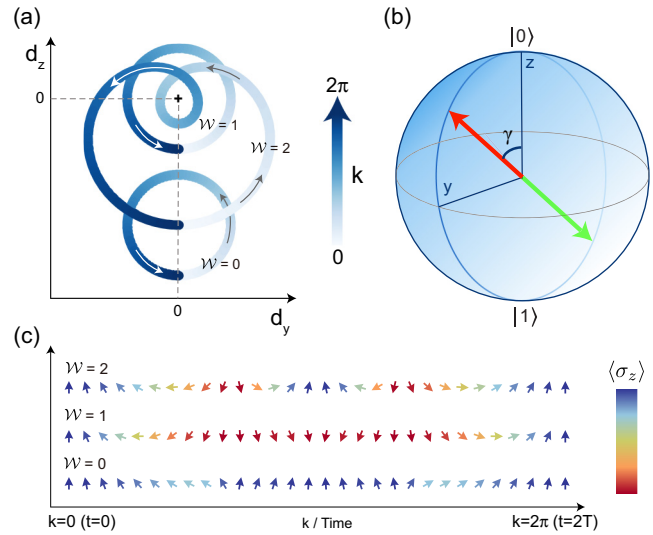

FIG. 1. Topological characteristics of the effective Hamiltonian of the Kitaev chain and the principle of simulation. (a) Trajectories of the Anderson pseudospin vector $\vec{d}(k)$ in different topological phases of the Kitaev chain as k is varied across the first Brillouin zone. The topological invariant of each phase is the winding number $\mathcal{W}$ of $\vec{d}(k)$ as defined in the main text. (b) Adiabatic evolution of a qubit driven by the Hamiltonian given in Eq. (2). The red and green arrows represent the two instantaneous eigenstates of $H(k(t))$, whose orientation is aligned with the red arrow. (c) Evolution of the qubit state in three different topological phases with $\mathcal{W} = 0, 1, 2$. The direction of the arrows indicates the orientation of the qubit in the yz plane of the Bloch sphere: Pointing upwards corresponds to the state $|0\rangle$, and downwards corresponds to $|1\rangle$. The number of completed circles of the qubit rotating in the yz plane of the Bloch sphere, as k is varied from 0 to 2π, is exactly the winding number $\mathcal{W}$ of the pesudospin $\vec{d}(k)$. The color gradient of $\langle \sigma_z \rangle$ will be used for better visualization of different topological phases in the figures presented later.

In the discussion above, adiabatic evolutions of the Hamiltonian were assumed in order to avoid unwanted transitions between its instantaneous eigenstates. However, the adiabatic condition requires a long runtime, which is not desirable due to finite decoherence times of our qubits. To overcome this problem, we employed a technique known as "shortcut to adiabaticity" (STA) [43] to accelerate the evolutions in our experiment. For the data reported here, $T = 200$ ns, so the longest evolution time corresponding to the case of $k = 2\pi$ is only 400 ns, which is more than two orders of magnitude shorter than a typical adiabatic evolution that can achieve the same goal. In other words, the STA acceleration is crucial for carrying out the experiment. Further discussion on this acceleration can be found in Appendix B.

III. EXPERIMENT

We used the Xmon type of superconducting qubits to carry out our simulation. All data reported in this work were acquired using one qubit, and similar results were reproduced on other qubits. The frequency of the qubit used here is around $\omega_{10}/2\pi = 5.42$ GHz and can be fine-tuned by a bias current on a Z control line. The relaxation and dephasing times are $T_1 = 10.4\,\mu$s, $T_2 = 2.4\,\mu$s, respectively. The external drive $\vec{B}$ is realized by applying microwave pulses of specific shapes through an XY control line. The qubit is capacitively coupled to a $\lambda/4$ resonator ($\omega_r/2\pi = 6.68$ GHz, with a coupling strength around 40 MHz), which is, in turn, coupled to a transmission line. The state of the qubit can be deduced by measuring the transmission coefficient S_{21} of the transmission line using the dispersive readout scheme. Further details of the samples can be found in Appendix A.

Figure 2(a) shows the experimental results for the case of having only the NN coupling ($\lambda_1 = 1$, $\lambda_2 = 0$). The state of the qubit, represented by arrows of different orientations, is plotted as a function of the chemical potential μ and momentum k. An arrow pointing upwards corresponds to $|0\rangle$; one pointing downwards corresponds to $|1\rangle$, and an arbitrary orientation corresponds to a linear superposition of $|0\rangle$ and $|1\rangle$. For each specific combination of (μ, k), the qubit was initialized to $|0\rangle$ at $t = 0$ ($k = 0$) and evolved under the Hamiltonian of Eq. (2) for a time interval of $t = kT/\pi$; then its state was determined by measuring $\langle\sigma_y\rangle$ and $\langle\sigma_z\rangle$, as discussed above. Therefore the direction of an arrow represents the orientation of the state vector of the qubit on the Bloch sphere at that specific combination of (μ, k).

In the absence of the NNN coupling ($\lambda_2 = 0$), the model described by Eq. (1) reduces to the original one-dimensional Kitaev chain. It has two topologically distinctive phases that correspond to the weak-pairing BCS regime ($|\mu| < 2\lambda_1$) and the strong-pairing Bose-Einstein condensate (BEC) regime ($|\mu| > 2\lambda_1$) [5]. The weak-pairing phase is topologically nontrivial and supports one Majorana zero-energy mode at each end of the chain, whereas the strong-pairing phase is topologically trivial and does not possess any Majorana zero-energy modes.

From the experimental data, two distinctive regimes of the parameter space can, indeed, be identified: $|\mu| > 2\lambda_1$ and $|\mu| < 2\lambda_1$ ($\lambda_1 = 1$ in Fig. 2). In the regime of $|\mu| > 2\lambda_1$, as k varies from 0 to π, the state vector of the qubit first rotates from $|0\rangle$ towards $|1\rangle$ but never reaches $|1\rangle$ and rotates back to $|0\rangle$. When k varies from π to 2π, the qubit basically repeats the above rotation, but in the opposite way. After one complete cycle, the qubit returns to the initial state of $|0\rangle$. The trajectory of the qubit during the cycle does not form a closed circle on the yz plane of the Bloch sphere. In other words, the winding number $\mathcal{W}$ is zero. This regime corresponds to the strong-pairing BEC phase of the Kitaev chain and is topologically trivial since $\mathcal{W} = 0$. On the other hand, for $|\mu| < 2\lambda_1$, it is obvious that the trajectory of the qubit does form a circle on the yz plane of the Bloch sphere as k varies from 0 to 2π. This regime thus corresponds to the weak-pairing BCS phase of the Kitaev chain and is topologically nontrivial, with $\mathcal{W} = 1$. Topological phase transitions occur as μ is varied across the borders of $\pm 2\lambda_1$. Figure 2(b) plots the winding number $\mathcal{W}$ extracted from data in Fig. 2(a). This plot gives a more direct

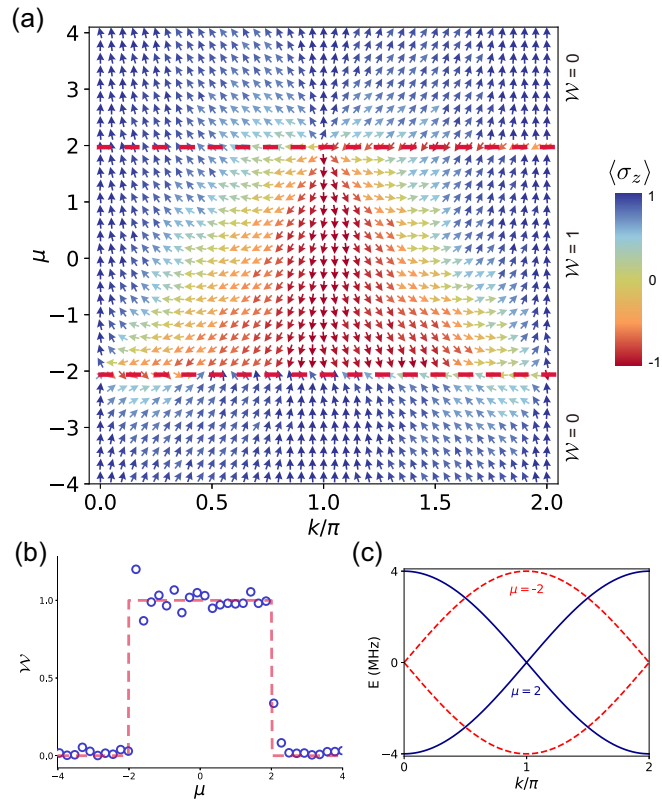

FIG. 2. Experimental data for the case with only NN coupling. For this specific measurement, we set $\lambda_1 = 1$, $\lambda_2 = 0$. Details of the measurement are described in the main text. (a) Evolution of the qubit as μ and k are varied. The meaning of the arrows and the color scheme are the same as in Fig. 1(c). The two dashed lines mark the μ values (± 2) where topological phase transitions occur as predicted by theory. (b) Winding number extracted from data in (a) using $\mathcal{W} = \oint d\theta(k)/2\pi$. For $\theta(k)$, we use the orientation angles of arrows in (a) since they are identical to the angle of $\vec{d}(k)$ as explained in the text. (c) Energy-momentum dispersion relation $E(k)$ at two different values of μ where topological phase transition occurs, as corroborated by the closing of the energy gap. $E(k)$ is deduced from the Rabi frequency of the microwave pulses used in measurements that produced data in (a). For a two-band model as in this case, the Rabi frequency gives the gap between the two symmetrically distributed energy bands.

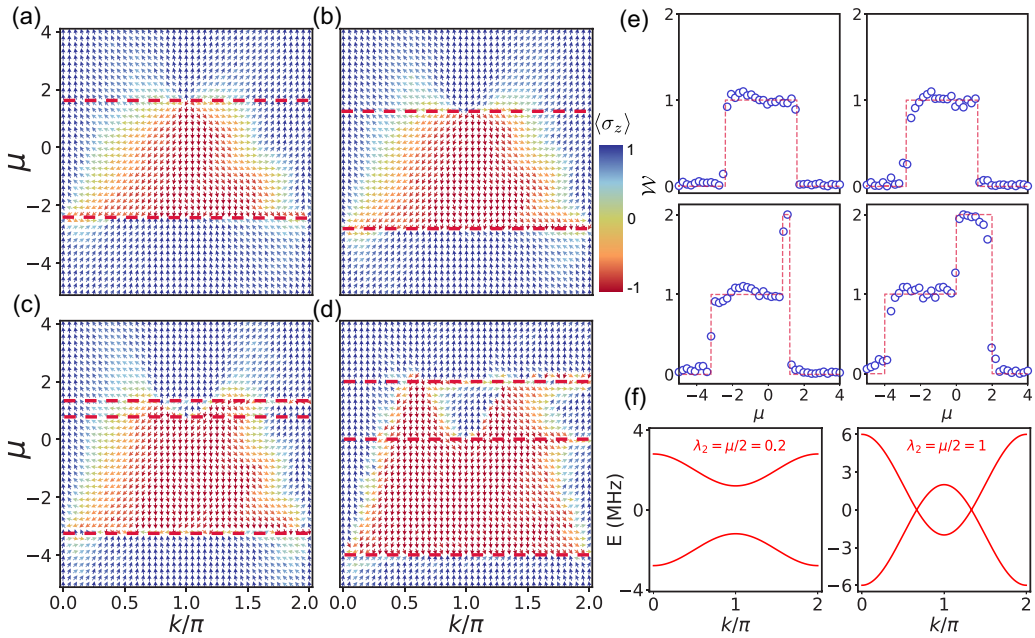

FIG. 3. Experimental data for the case with both NN and NNN coupling. Here $\lambda_1 = 1$, and $\lambda_2 = 0.2, 0.4, 0.6, 1.0$ for (a)–(d), respectively. In (a) and (b), where $\lambda_2 < 0.5\lambda_1$, only two distinctive topological phases ($\mathcal{W} = 0$ and 1) are present. In (c) and (d), where $\lambda_2 > 0.5\lambda_1$, a third phase of $\mathcal{W} = 2$ emerges. (e) Winding numbers extracted for the data in (a)–(d) using the same method as in Fig. 2(b). (f) Energy-momentum dispersion relation $E(k)$ of two representative cases: Away from (left) and the occurrence of (right) phase transition. $E(k)$ is deduced from the Rabi frequency of microwave pulses that are used for obtaining the data in (a) and (d).

and simple demonstration of the topological phase transitions in this case. In Fig. 2(c), the energy bands deduced from one experimental control parameter, the Rabi frequency of the microwave pulses, are plotted. It is obvious that topological phase transitions occur only when the energy gap closes.

Next, we extended our simulation to include the NNN coupling λ_2. We fixed the NN coupling strength to be $\lambda_1 = 1$ and measured the state of the qubit as λ_2, μ, and k were varied. Figures 3(a)–3(d) show the results for four representative values of λ_2. At $\lambda_2 = 0$ (not shown in Fig. 3), the model described by Eq. (1) simply reduces to the case of only having the NN coupling, as shown in Fig. 2. As λ_2 increases but is still smaller than $0.5\lambda_1$ [Figs. 3(a) and 3(b)], the system continues to have only two topological phases ($\mathcal{W} = 0$ or 1). However, the phase transitions now occur at $\mu = -2\lambda_1 - 2\lambda_2$ and $\mu = 2\lambda_1 - 2\lambda_2$. Once λ_2 reaches $0.5\lambda_1$, a third phase with $\mathcal{W} = 2$ emerges, as shown in Figs. 3(c) and 3(d). When $\mu < -2\lambda_1 - 2\lambda_2$, the system is in a topologically trivial phase with $\mathcal{W} = 0$. As μ increases, the system first undergoes a transition to a phase of $\mathcal{W} = 1$ at $\mu = -2\lambda_1 - 2\lambda_2$ and then another transition to a phase of $\mathcal{W} = 2$ at $\mu = 2\lambda_1 - 2\lambda_2$. Finally, when $\mu > 2\lambda_2$, the system undergoes yet another transition to the phase of $\mathcal{W} = 0$. Such phase transitions become more obvious in the plots of extracted winding numbers shown in Fig. 3(e). The two plots of energy bands in Fig. 3(f) correspond to the data in Figs. 3(a) and 3(d), again demonstrating that phase transitions occur only when the energy gap closes.

Due to the interplay of multiple parameters of λ_1, λ_2, and μ, the phase diagram of the Kitaev chain with long-range coupling is rather sophisticated. Nevertheless, by carefully designing the control microwave pulses, we are able to map out its enriched phase diagram. Without loss of generality, Fig. 4 shows such phase diagram for a specific case of $\mu = -2$. Figures 4(a)–4(c) show the measured state of the qubit as a function of λ_2 and k at three representative λ_1 values. In each case, multiple phases with different topological invariants can be identified. Figure 4(d) aggregates experimental data taken at a collection of λ_1 values. The evolution of the boundaries between different phases can clearly be seen. In particular, two quantum multicritical points can be identified where three different topological phases coexist. The phase diagram obtained experimentally agrees with the theoretical result very well [6–8].

IV. SUMMARY AND DISCUSSION

In summary, we have simulated the topological phase transition in the Kitaev chain with both NN and NNN coupling using superconducting quantum circuits. By mapping the effective Hamiltonian of the system in the momentum space onto that of a qubit driven by a tunable control field, we produce intuitive visualization of different topological phases. The much enhanced efficiency of measurement makes it possible to obtain a comprehensive phase diagram covering a wide range of the parameter space. Topological phase transitions and quantum multicritical points are clearly demonstrated. In particular, new topological phases due to long-range coupling are observed.

The method used in this work represents a simple yet versatile way of simulating quantum phase transitions in various topological matters and can be easily generalized to study more complex systems with higher spatial dimensions and more complex couplings, such as power-law decaying pairing [11,16,44]. The current technique can also be used to

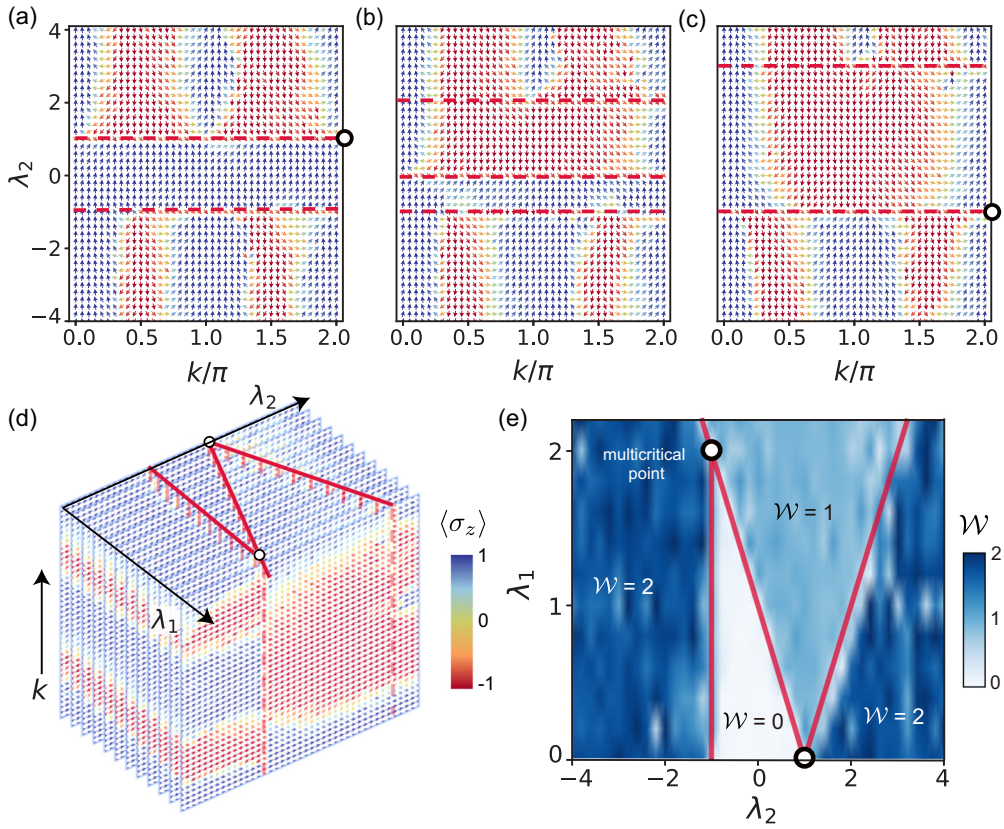

FIG. 4. Quantum phase diagram and multicritical points of the Kitaev chain with NN and NNN coupling. Here $\lambda_1 = 0, 1, 2$ for (a)–(c), respectively. (d) Aggregation of experimental data for different λ_1 values. Solid red lines mark the evolution of phase boundaries. (e) Comparison of experimentally obtained and theoretically predicted phase diagrams. Solid red lines and $\mathcal{W}$ values in the text are theoretical predictions. In all panels, black circles mark the quantum multicritical points where three phases coexist.

study nonequilibrium dynamics of certain systems, including, for example, Floquet engineering of the Kitaev chain where the chemical potential and pairing strength are time dependent [45,46] and dynamical quantum phase transitions [47]. Moreover, topological systems at finite temperatures may be simulated with this technique as well [48,49].

Since the current method relies on the effective Hamiltonian in the k space of the system under study, in general it is not applicable to systems with interaction. However, we do want to point out that under certain circumstances, an interacting system may also be described by decoupled modes in k space [50], thus becoming simulatable with the current method. More generally, as long as a system can be described by some effective Hamiltonian in k space, the complexity of simulating the system has already been largely reduced. In those cases, the current technique, together with a straightforward generalization to multiple qubits, can be very useful. Another interesting extension may be the construction and simulation of $H(k)$ under various constraints of symmetry via direct k-space engineering [51] and studying the topological phases of the resultant systems.

ACKNOWLEDGMENTS

This work was supported by the Key-Area Research and Development Program of Guangdong Province (Grant No. 2018B030326001), the National Natural Science Foundation of China (Grant No. U1801661), the Guangdong Innovative and Entrepreneurial Research Team Program (Grant No. 2016ZT06D348), the Natural Science Foundation of Guangdong Province (Grant No. 2017B030308003), and the Science, Technology and Innovation Commission of Shenzhen Municipality (Grants No. ZDSYS20170303165926217, No. JCYJ20170412152620376, No. KYTDPT20181011104202253).

APPENDIX A: SAMPLE INFORMATION

Figure 5 shows optical images of one of the samples used in this work. The Xmon qubit consists of a superconducting quantum interference device loop with two symmetrically designed Josephson junctions. The magnetic flux piercing the loop can be fine-tuned by a bias current flowing through the Z control line, which can adjust the spacing between the energy levels of the qubit. Microwave control pulses are applied to the qubit via an XY control line that is capacitively coupled to the qubit.

APPENDIX B: MICROWAVE CONTROL AND STA ACCELERATION

The effective Hamiltonian of a microwave-driven qubit in the rotating frame is given by

$$H_0(t) = \frac{\hbar}{2}\begin{pmatrix} \Delta & \Omega_M e^{-i\phi} \\ \Omega_M e^{i\phi} & -\Delta \end{pmatrix}, \tag{B1}$$

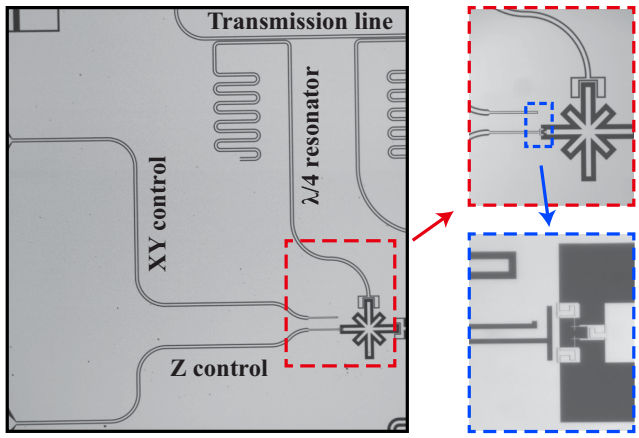

FIG. 5. Optical images of an Xmon qubit used in this work.

where Ω_M, Δ, ϕ are the frequency, detuning, and phase of the envelope of the control microwave pulse, respectively. It can be written in terms of Pauli matrices $\vec{\sigma} = (\sigma_x, \sigma_y, \sigma_z)$: $H_0(t) = \frac{\hbar}{2}\vec{B}(t)\cdot\vec{\sigma}$. Here the effective control field $\vec{B} = |B|(\sin\theta\cos\phi, \sin\theta\sin\phi, \cos\theta)$, and $|B|$ is equal to the Rabi frequency $\Omega = \sqrt{\Omega_M^2 + \Delta^2}$ and $\tan\theta = \Omega_M/\Delta$. The instantaneous eigenstates of $H_0(t)$ are $|\psi_+\rangle = \cos\frac{\theta}{2}|0\rangle + \sin\frac{\theta}{2}e^{i\phi}|1\rangle$ and $|\psi_-\rangle = -\sin\frac{\theta}{2}e^{-i\phi}|0\rangle + \cos\frac{\theta}{2}|1\rangle$.

By setting $\phi = \pi/2$ and tuning $\Omega_M(t)$ and $\Delta(t)$, the Hamiltonian described by Eq. (B1) can be used to simulate the effective Hamiltonian of the Kitaev chain in the momentum space. One example is given in Fig. 6(c), where $\Omega_M(t)$ and $\Delta(t)$ are plotted as functions of a normalized time t/T for parameters $(\lambda_1, \lambda_2, \mu) = (1, 0, 1.8)$. A proper choice of T has to take into account several factors such as anharmonicity of qubits and adiabaticity of evolutions.

For the adiabaticity issue, as discussed in the main text, it is usually required to drive a qubit to evolve adiabatically. In other words, the evolutions must be kept slow enough to avoid unwanted transitions between the instantaneous eigenstates of the qubit. In order to find the proper time of evolution, we run numerical simulations to study how the qubit evolves at different values of T. A representative result is shown in Fig. 6(d), where $\langle\sigma_z\rangle$ of the qubit during evolution is plotted for different T. It is obvious that at short T (for example, $6\,\mu$s), the behavior of the qubit deviates from adiabatic evolution significantly. Only when T is close to $30\,\mu$s (corresponding to a total evolution time of $2T = 60\,\mu$s) can one observe reasonable behavior of the qubit approaching an adiabatic evolution. Given the finite decoherence times of our qubits, it is impossible to run our experiments with such long evolution times. In fact, even with the best superconducting qubits available today, running the experiment without any kind of acceleration would still make it difficult, if not impossible, to produce a data set of similar quality and to be comprehensive enough for generating the phase diagram shown in the main text.

Various STA techniques have been proposed and implemented to accelerate adiabatic processes (for a general review on this topic, see Ref. [52]). One way to implement STA is known as counterdiabatic driving [43], which is used in the current work and will be discussed in the following.

The essential idea of STA is to include an auxiliary term $H_a(t)$ in the original Hamiltonian $H_0(t)$: $H_{STA}(t) = H_0(t) + H_a(t)$, so that the temporal dynamics of $H_{STA}(t)$ are equivalent

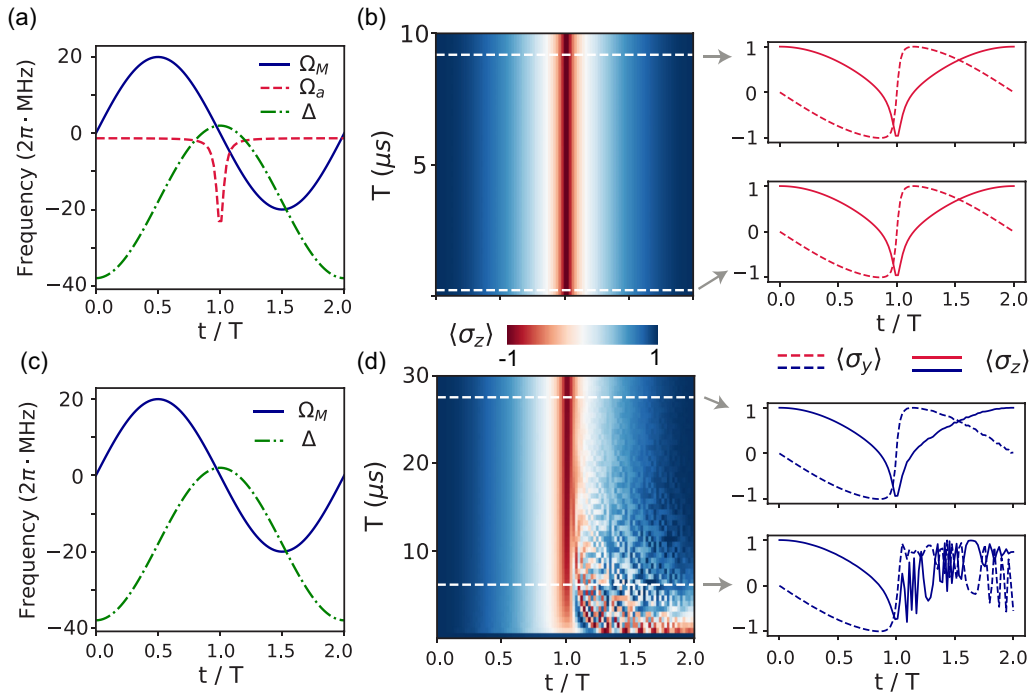

FIG. 6. (a) Frequency $\Omega_M(t)$, auxiliary frequency $\Omega_a(t)$, and detuning $\Delta(t)$ of the envelope of the microwave control pulse with STA. (c) $\Omega_M(t)$ and $\Delta(t)$ of the envelope of the microwave control pulse without STA. Numerical simulations of $\langle\sigma_z\rangle$ at different values of T, (b) with and (d) without STA. For all panels, we use the parameter set $(\lambda_1, \lambda_2, \mu) = (1, 0, 1.8)$.

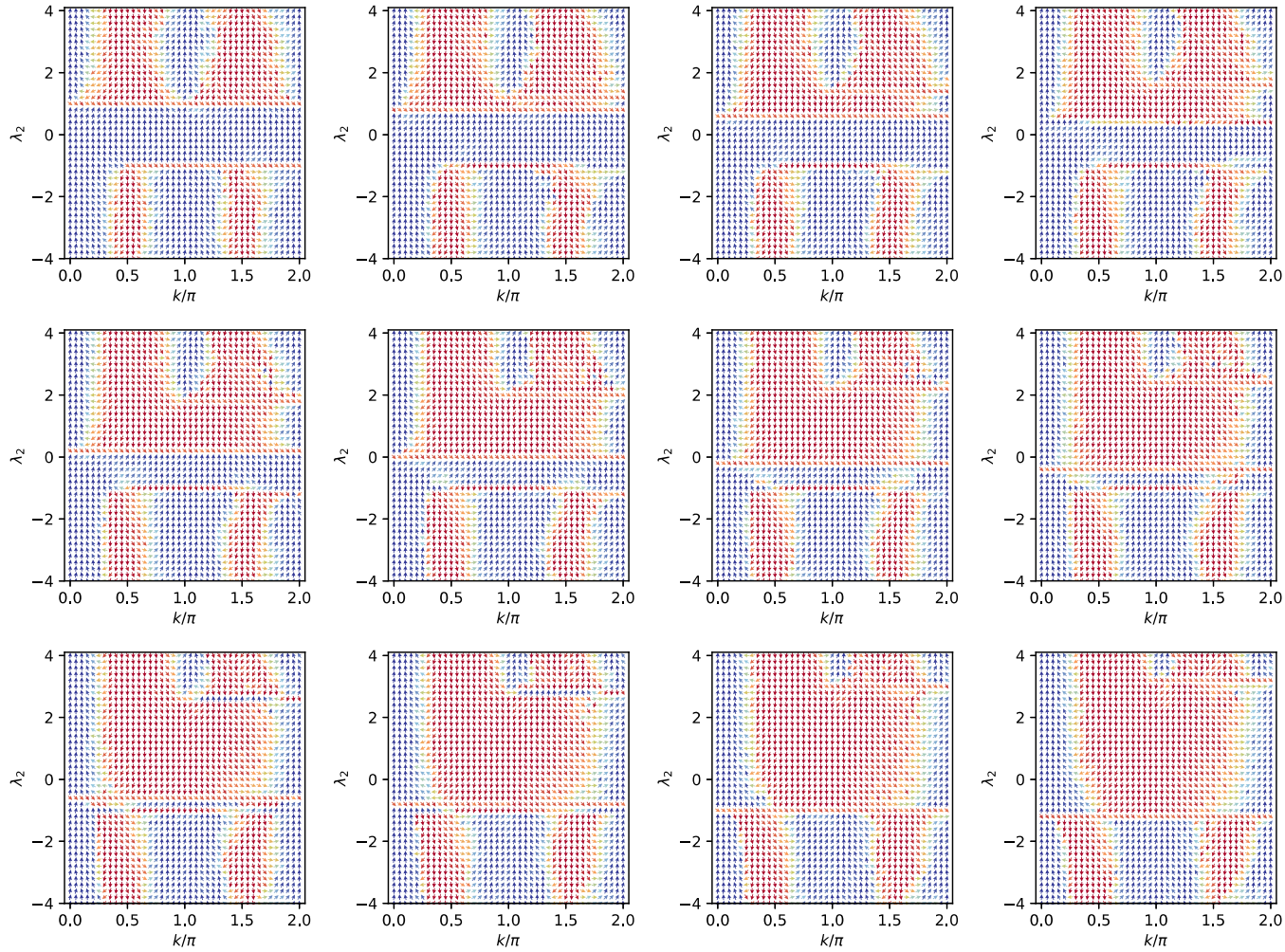

FIG. 7. Detailed data used in Fig. 4 in the main text. $\lambda_1 = 0.0, 0.2, 0.4, \ldots, 2.2$ from left to right and top to bottom.

to adiabatic evolutions of the original Hamiltonian $H_0(t)$ even on a short timescale. The specific form of $H_a(t)$ can be found via different approaches based on, for example, dressed states and dynamical invariants. In this experiment, we used $H_a(t) = i\Omega_a(e^{i\phi}|1\rangle\langle 0| + e^{-i\phi}|0\rangle\langle 1|)$ with an auxiliary frequency $\Omega_a = \dot{\theta}$. Figure 6(a) plots the relevant parameters as functions of a normalized time t/T for parameters $(\lambda_1, \lambda_2, \mu) = (1, 0, 1.8)$ [similar to Fig. 6(c)]. Figure 6(b) plots results of numerical simulations of $\langle\sigma_z\rangle$ at different values of T [similar to Fig. 6(d)], but now with the STA acceleration applied. It is obvious that, with STA, evolution of the qubit can be effectively adiabatic even for a T as short as 200 ns, which is about an order of magnitude shorter than the decoherence times of our qubits and more than two orders of magnitude shorter than the required time of evolution in the case without STA.

In short, STA acceleration is crucial for carrying out the experiment in this work. Without it, it is impossible to obtain the comprehensive phase diagram reported here.

APPENDIX C: SUPPLEMENTAL DATA FOR THE QUANTUM PHASE DIAGRAM

Figure 7 plots detailed data used in Fig. 4 in the main text for generating the phase diagram. In each panel, at certain values of λ_2, strange behavior of the qubit evolution can be identified. Such phenomena are a herald of quantum phase transitions. At these values of λ_2, the two energy bands of the effective Hamiltonian $H(k)$ touch each other (closing the gap) at certain values of k, and the winding number of the Anderson pseudospin $\vec{d}(k)$ becomes ill defined, thus the strange behavior of the qubit evolution.

[1] A. Y. Kitaev, Phys. Usp. **44**, 131 (2001).
[2] Edited by H. Luo, *Advanced Topological Insulators*, Advanced Material Series (Martin Scrivener and Phillip Carmical, Beverly, MA, 2019).
[3] T. Ozawa, H. M. Price, A. Amo, N. Goldman, M. Hafezi, L. Lu, M. C. Rechtsman, D. Schuster, J. Simon, O. Zilberberg, and I. Carusotto, Rev. Mod. Phys. **91**, 015006 (2019).
[4] N. Read and D. Green, Phys. Rev. B **61**, 10267 (2000).

[5] J. Alicea, Rep. Prog. Phys. **75**, 076501 (2012).
[6] A. Kopp and S. Chakravarty, Nat. Phys. **1**, 53 (2005).
[7] Y. Niu, S. B. Chung, C.-H. Hsu, I. Mandal, S. Raghu, and S. Chakravarty, Phys. Rev. B **85**, 035110 (2012).
[8] G. Zhang and Z. Song, Phys. Rev. Lett. **115**, 177204 (2015).
[9] W. DeGottardi, M. Thakurathi, S. Vishveshwara, and D. Sen, Phys. Rev. B **88**, 165111 (2013).
[10] F. Pientka, L. I. Glazman, and F. von Oppen, Phys. Rev. B **88**, 155420 (2013).
[11] D. Vodola, L. Lepori, E. Ercolessi, A. V. Gorshkov, and G. Pupillo, Phys. Rev. Lett. **113**, 156402 (2014).
[12] A. Ghazaryan and T. Chakraborty, Phys. Rev. B **92**, 115138 (2015).
[13] D. Vodola, L. Lepori, E. Ercolessi, and G. Pupillo, New J. Phys. **18**, 015001 (2015).
[14] Z. C. Shi, X. Q. Shao, Y. Xia, and X. X. Yi, Phys. Lett. A **381**, 3043 (2017).
[15] F. Pientka, Y. Peng, L. Glazman, and F. von Oppen, Phys. Scr. **T164**, 014008 (2015).
[16] O. Viyuela, D. Vodola, G. Pupillo, and M. A. Martin-Delgado, Phys. Rev. B **94**, 125121 (2016).
[17] L. Lepori and L. Dell'Anna, New J. Phys. **19**, 103030 (2017).
[18] K. Patrick, T. Neupert, and J. K. Pachos, Phys. Rev. Lett. **118**, 267002 (2017).
[19] A. Alecce and L. Dell'Anna, Phys. Rev. B **95**, 195160 (2017).
[20] A. Zazunov, F. Buccheri, P. Sodano, and R. Egger, Phys. Rev. Lett. **118**, 057001 (2017).
[21] A. Trenkwalder, G. Spagnolli, G. Semeghini, S. Coop, M. Landini, P. Castilho, L. Pezzè, G. Modugno, M. Inguscio, A. Smerzi, and M. Fattori, Nat. Phys. **12**, 826 (2016).
[22] R. Islam, E. Edwards, K. Kim, S. Korenblit, C. Noh, H. Carmichael, G.-D. Lin, L.-M. Duan, C.-C. J. Wang, J. Freericks, and C. Monroe, Nat. Commun. **2**, 377 (2011).
[23] K. Kim, M.-S. Chang, S. Korenblit, R. Islam, E. E. Edwards, J. K. Freericks, G.-D. Lin, L.-M. Duan, and C. Monroe, Nature (London) **465**, 590 (2010).
[24] R. Gerritsma, G. Kirchmair, F. Zähringer, E. Solano, R. Blatt, and C. F. Roos, Nature (London) **463**, 68 (2010).
[25] A. Friedenauer, H. Schmitz, J. T. Glueckert, D. Porras, and T. Schaetz, Nat. Phys. **4**, 757 (2008).
[26] J. Zhang, X. Peng, N. Rajendran, and D. Suter, Phys. Rev. Lett. **100**, 100501 (2008).
[27] P. Roushan, C. Neill, A. Megrant, Y. Chen, R. Babbush, R. Barends, B. Campbell, Z. Chen, B. Chiaro, A. Dunsworth, A. Fowler, E. Jeffrey, J. Kelly, E. Lucero, J. Mutus, P. J. J. O'Malley, M. Neeley, C. Quintana, D. Sank, A. Vainsencher *et al.*, Nat. Phys. **13**, 146 (2017).
[28] P. Roushan, C. Neill, J. Tangpanitanon, V. M. Bastidas, A. Megrant, R. Barends, Y. Chen, Z. Chen, B. Chiaro, A. Dunsworth, A. Fowler, B. Foxen, M. Giustina, E. Jeffrey, J. Kelly, E. Lucero, J. Mutus, M. Neeley, C. Quintana, D. Sank *et al.*, Science **358**, 1175 (2017).
[29] K. Xu, J.-J. Chen, Y. Zeng, Y.-R. Zhang, C. Song, W. Liu, Q. Guo, P. Zhang, D. Xu, H. Deng, K. Huang, H. Wang, X. Zhu, D. Zheng, and H. Fan, Phys. Rev. Lett. **120**, 050507 (2018).
[30] D.-W. Wang, C. Song, W. Feng, H. Cai, D. Xu, H. Deng, H. Li, D. Zheng, X. Zhu, H. Wang, S.-Y. Zhu, and M. O. Scully, Nat. Phys. **15**, 382 (2019).
[31] P. Roushan, C. Neill, Y. Chen, M. Kolodrubetz, C. Quintana, N. Leung, M. Fang, R. Barends, B. Campbell, Z. Chen, B. Chiaro, A. Dunsworth, E. Jeffrey, J. Kelly, A. Megrant, J. Mutus, P. J. J. O'Malley, D. Sank, A. Vainsencher, J. Wenner *et al.*, Nature (London) **515**, 241 (2014).
[32] X. Tan, Y. Zhao, Q. Liu, G. Xue, H. Yu, Z. D. Wang, and Y. Yu, npj Quantum Mater. **2**, 60 (2017).
[33] X. Tan, D.-W. Zhang, Q. Liu, G. Xue, H.-F. Yu, Y.-Q. Zhu, H. Yan, S.-L. Zhu, and Y. Yu, Phys. Rev. Lett. **120**, 130503 (2018).
[34] X. Tan, Y. X. Zhao, Q. Liu, G. Xue, H.-F. Yu, Z. D. Wang, and Y. Yu, Phys. Rev. Lett. **122**, 010501 (2019).
[35] M. D. Schroer, M. H. Kolodrubetz, W. F. Kindel, M. Sandberg, J. Gao, M. R. Vissers, D. P. Pappas, A. Polkovnikov, and K. W. Lehnert, Phys. Rev. Lett. **113**, 050402 (2014).
[36] W. Ma, L. Zhou, Q. Zhang, M. Li, C. Cheng, J. Geng, X. Rong, F. Shi, J. Gong, and J. Du, Phys. Rev. Lett. **120**, 120501 (2018).
[37] K. Yang, L. Zhou, W. Ma, X. Kong, P. Wang, X. Qin, X. Rong, Y. Wang, F. Shi, J. Gong, and J. Du, Phys. Rev. B **100**, 085308 (2019).
[38] Y. Wang, W. Ji, Z. Chai, Y. Guo, M. Wang, X. Ye, P. Yu, L. Zhang, X. Qin, P. Wang, F. Shi, X. Rong, D. Lu, X.-J. Liu, and J. Du, Phys. Rev. A **100**, 052328 (2019).
[39] C. Schneider, D. Porras, and T. Schaetz, Rep. Prog. Phys. **75**, 024401 (2012).
[40] J. W. Britton, B. C. Sawyer, A. C. Keith, C.-C. J. Wang, J. K. Freericks, H. Uys, M. J. Biercuk, and J. J. Bollinger, Nature (London) **484**, 489 (2012).
[41] P. Jurcevic, B. P. Lanyon, P. Hauke, C. Hempel, P. Zoller, R. Blatt, and C. F. Roos, Nature (London) **511**, 202 (2014).
[42] A. Bermudez, T. Schaetz, and M. B. Plenio, Phys. Rev. Lett. **110**, 110502 (2013).
[43] X. Chen, I. Lizuain, A. Ruschhaupt, D. Guéry-Odelin, and J. G. Muga, Phys. Rev. Lett. **105**, 123003 (2010).
[44] A. Dutta and A. Dutta, Phys. Rev. B **96**, 125113 (2017).
[45] M. Benito, A. Gómez-Léon, V. M. Bastidas, T. Brandes, and G. Platero, Phys. Rev. B **90**, 205127 (2014).
[46] Z.-Z. Li, C.-H. Lam, and J. Q. You, Phys. Rev. B **96**, 155438 (2017).
[47] X.-Y. Guo, C. Yang, Y. Zeng, Y. Peng, H.-K. Li, H. Deng, Y.-R. Jin, S. Chen, D. Zheng, and H. Fan, Phys. Rev. Appl. **11**, 044080 (2019).
[48] O. Andersson, I. Bengtsson, M. Ericsson, and E. Sjöqvist, Philos. Trans. R. Soc. A **374**, 20150231 (2016).
[49] U. Bhattacharya and A. Dutta, Phys. Rev. B **97**, 214505 (2018).
[50] J.-J. Miao, H.-K. Jin, F.-C. Zhang, and Y. Zhou, Phys. Rev. Lett. **118**, 267701 (2017).
[51] S. Rahul, R. Ranjith Kumar, Y. R. Kartik, A. Banerjee, and S. Sarkar, Phys. Scr. **94**, 115803 (2019).
[52] E. Torrontegui, S. Ibáñez, S. Martínez-Garaot, M. Modugno, A. del Campo, D. Guéry-Odelin, A. Ruschhaupt, X. Chen, and J. G. Muga, Adv. At., Mol., Opt. Phys. **62**, 117 (2013).